CrossMark

Nanoscale hygromechanical behavior of lignin

Kristen M. Hess · Jason P. Killgore · Wil V. Srubar III

Abstract The nanoscale hygromechanical behavior of lignin is presented in this work. Three atomic force microscopy experimental methods were used to correlate moisture sorption of lignin to its mechanical behavior. First, sorption isotherms were established using cantilever mass sensing and subsequently predicted using the Guggenheim–Anderson–de Boer model. The sorption isotherms of lignin particles followed a repeatable and cyclic trend reaching a maximum moisture content of $\approx$ 17% at $\approx$ 79% relative humidity (RH). Second, 3D nanomechanical contrast images were obtained using contact resonance force microscopy (CR-FM) to observe the hygromechanical response of lignin over three RH cycles. Finally, force volume mapping and the Hertz model were used to compute the elastic modulus of lignin as a function of moisture content. As RH increased, CR-FM measurements revealed initial topographical heterogeneity, as well as notable surface softening, especially in initially smooth domains. The average elastic modulus of the smooth domain decreased from 9.0 to 4.3 to 2.4 GPa as the moisture content increased from 0.024 to 9.1 to 17.3%, respectively. Cyclic measurements confirm that the elastic modulus of lignin rebounds upon moisture desorption.

Introduction

Lignin, the most abundant natural aromatic polymer, is a readily available yet underutilized by-product of the papermaking and biofuel industries (Faruk and Sain 2016; Ragauskas et al. 2014; Lora 2008). The lignocellulosic feedstock has three main components, lignin, hemicellulose, and cellulose, where lignin constitutes 15%–30% by mass depending on the plant species (Faruk and Sain 2016; Ragauskas et al. 2014; Gellerstedt and Henriksson 2008; Fengel and Wegener 1983). The global pulp and papermaking industry produces a reported 70 million tons of extracted lignin each year, but only 2% (mostly lignosulfonates) is recovered for higher value utilization, while the

K. M. Hess · W. V. Srubar III (✉)
Department of Civil Environmental and Architectural
Engineering, University of Colorado Boulder, ECOT 441
UCB 428, Boulder, CO 80309-0428, USA
e-mail: wsrubar@colorado.edu

J. P. Killgore
Applied Chemicals and Materials Division, National
Institute of Standards and Technology, Boulder,
CO 80305, USA

remaining lignin is burned for internal energy generation (Costello 2017; Lora 2008). When using lignocellulosic biomass to produce ethanol, modern biofuel processing facilities generate a predicted 60% more lignin than needed to meet internal energy demands (Ragauskas et al. 2014; Sannigrahi and Ragauskas 2011; Sannigrahi et al. 2010; Lora 2008). The abundance of industrial lignin from these waste streams coupled with desirable attributes, such as low cost, low density, antimicrobial and antioxidant properties, biorenewability, and non-toxicity (Faruk and Sain 2016; Ragauskas et al. 2014; Thakur et al. 2014; Gandini and Belgacem 2008), presents a valuable opportunity to develop future products and technology.

Currently, the applications for lignin are limited but diverse. Lignin has been used as a binder for animal feed, an ingredient for pesticides, dispersants for oil well drilling products, emulsifiers, polyurethane foams, a resin component in wood panel products, and as a filler in inks and paints (Lupoi et al. 2015; Ragauskas et al. 2014; Lora 2008). More recently, lignin has shown promise as a chemical sensor (Faria et al. 2012), a nanocontainer for chemical delivery (Yiamsawas et al. 2014), a reinforcement for polymer composites (Faruk and Sain 2016), and a precursor for carbon fiber (Bajpai 2017; Brodin et al. 2012).

Lignin has a highly complex structure that can vary depending on plant source and more significantly due to the industry specific extraction method (Faruk and Sain 2016; Uraki and Koda 2015; Gandini and Belgacem 2008; Fengel and Wegener 1983). Despite the inherent variability, all lignin is comprised of three major structures, namely hydroxyphenyl, guaiacyl, and syringyl phenylpropanoid units, that form a three-dimensional irregular polymer (Faruk and Sain 2016; Ragauskas et al. 2014; Boerjan et al. 2003; Hatakeyama and Hatakeyama 2009; Sarkanen and Ludwig 1971). The reactive functional groups of lignin (e.g., phenolic and aliphatic hydroxyl groups) present a marked potential for chemical modification, but also a susceptibility to moisture (Fang and Smith 2016; Yiamsawas et al. 2014; Gandini and Belgacem 2008). Compared to other biopolymers, lignin demonstrates greater moisture resistance due to the phenyl groups found on its basic chain unit. However, lignin also has enough hydroxyl groups to interact with water molecules. In the presence of moisture, the water molecules break the hydrogen bonds between lignin molecules and form separate hydrogen bonds with any available lignin hydroxyl site (i.e., bound water). Once the sites are saturated, additional water molecules tend to aggregate through intermolecular hydrogen bonding (i.e., free water) (Hatakeyama et al. 1983; Hatakeyama and Hatakeyama 2009; Vu et al. 2002; Charlier and Mazeau 2012; Youssefian et al. 2017). This physiochemical explanation of the molecular interaction between lignin and water suggests a corresponding hygromechanical response.

In previous studies, lignin moisture sorption isotherms have been experimentally determined using dynamic vapor sorption (Volkova et al. 2012) and gravitational methods (Chirkova et al. 2009; Bouajila et al. 2006; Reina et al. 2001; Cousins 1976; Engelund 2011) or computationally predicted using moisture sorption models such as the Bruanauer–Emmett–Teller (BET) (Bouajila et al. 2006; Volkova et al. 2012), Guggenheim–Anderson–de Boer (GAB) (Volkova et al. 2012), and D'Arcy and Watt (Reina et al. 2001) models. In a previous study, atomic force microscopy (AFM) measurements showed that lignin-rich cell walls have improved nanomechanical properties (e.g., elastic modulus) compared to delignified cellulose-rich walls (Farahi et al. 2017). However, experimental results relating the elastic modulus and moisture content of extracted lignin are largely limited to studies conducted in the late 1970s by Cousins (Cousins 1976, 1977). In this previous work, the specimens were molded from powdered lignin and subsequently exposed to different increasing relative humidity (RH) conditions. The specimens were then removed from the specific RH conditions to an ambient laboratory where tensile and indentation tests were performed using rod or disk specimens, respectively. The notable limitations of this experimental approach are threefold. First, specimens are removed from RH conditions then mechanically tested. Second, the mechanical response cannot be characterized for cycles of RH due to the nature of destructive testing and utilization of RH chambers regulated using salt solutions. Third, specimens are subjected to high temperature and compressive force conditions during preparation, which may affect the mechanical response. To the authors' knowledge, the hygromechanical properties of lignin have not since been experimentally investigated as substantiated by the continual use of Cousins results in the literature

(Youssefian et al. 2017; Kulasinski et al. 2015; Célino et al. 2014).

Scope of work

It is proposed that the hygromechanical behavior of lignin can be characterized on the nanoscale using atomic force microscopy (AFM) techniques. AFM was first designed to capture high resolution topographical images of a material surface on the nanoscale (Binnig et al. 1986). The potential was quickly recognized for deriving nanomechanical property data, such as elastic modulus, from the cantilever tip-surface interaction, and AFM techniques have since been developed and successfully implemented (Maivald et al. 1991; Troyon et al. 1997; Vairac and Cretin 1998; Rosa-Zeiser et al. 1997).

To address the limitations of previous work by Cousins (1976, 1977), this study leverages three AFM techniques to relate moisture content and nanoscale mechanical properties, namely elastic modulus, of lignin. First, the AFM cantilever, which acts as a microscale mass balance, was vibrated with a lignin particle attached to the cantilever tip for multiple cycles of RH. The increase or decrease in computed mass corresponding to the RH condition was attributed to the moisture content of the lignin particle. Second, contact resonance force microscopy (CR-FM) AFM measurements were taken as RH increased and decreased to identify nanomechanical contrast over the surface of lignin due to topographical heterogeneity and moisture content. Finally, AFM force spectroscopy measurements were completed at increasing and decreasing RH increments to compute the elastic modulus of lignin as it relates to moisture content. In this study, a series of AFM techniques were (1) performed using the same experimental set-up to control RH were and (2) used to investigate the moisture sorption and corresponding hygromechanical response of extracted lignin on the single-particle and particle-surface length scales, respectively (Fig. 1).
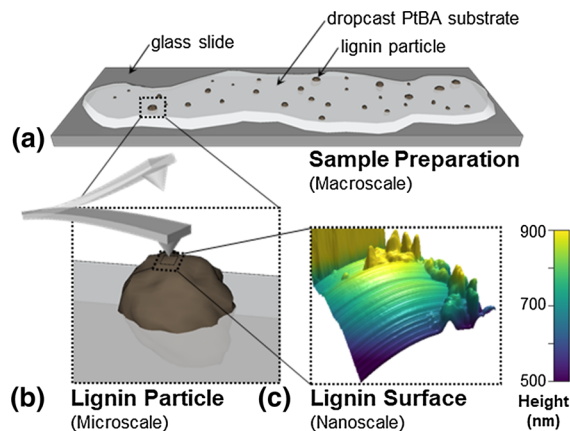

Fig. 1 Length-scale schematic for AFM measurements. During sample preparation **a** lignin particles were partially embedded within a poly(tert-butyl acrylate) (PtBA) substrate. During AFM scanning, **b** the PtBA substrate secured the lignin particles in place. A 3D topographical AFM scan of the lignin particle surface, **c** is shown for reference

Materials and methods[1]

Material

The primary material used for this study is alkali lignin with low sulfonate (CAS Number 8068-05-1, Lot Number 04414PEV, Sigma Aldrich), which is in powdered form with microscale particle aggregates. Documentation from Sigma Aldrich reports an average molecular weight of $\sim 10{,}000$ and no reducing sugars contained within the product. The molecular weight was experimentally confirmed by size exclusion chromatography, as shown in Supplementary Fig. 1. According to a sieve analysis of alkali lignin, 0% of the particles are > 250 μm, $\approx 30\%$ of the particles are between 250 and 125 μm, and $\approx 70\%$ of the particles are < 125 μm. Other materials used for this study include toluene (CAS Number 108-88-3, Sigma Aldrich), poly(tert-butyl acrylate) (Cat Number 18240, Polysciences, Inc.), 2.0 mm transparent polystyrene sheet (Product Number ST313200, Goodfellow), and ultra-violet light activated clear finish adhesive (Loon Outdoors).

---

[1] Commercial equipment, instruments, or materials are identified only in order to adequately specify certain procedures. In no case does such identification imply recommendation or endorsement by the National Institute of Standards and Technology, nor does it imply that the products identified are necessarily the best available for the purpose.

Atomic force microscopy (AFM)

Experimental set-up

All AFM measurements were conducted at room temperature ($\approx$ 18 °C) using a MFP-3D AFM (Asylum Research, Santa Barbara, CA) equipped with a humidity sensing cell accessory (Model HUMIDSC, Asylum Research). RH within the cell was controlled by flowing a mixture of dry and saturated gas through one of the access ports. The gas was saturated by flowing through a series of two bubblers filled with water. Two MC standard series mass flow controllers (Alicat Scientific, Tucson, AZ) varied the flow rates from the dry and saturated gas lines, respectively, to the humidity sensing cell, to obtain RH conditions between $\approx$ 0 and $\approx$ 80%.

Determining the moisture content of lignin particles using a cantilever mass sensor

Lignin particles were distributed on a glass slide and a single drop of UV-curable adhesive was spread on a separate glass slide. Before the cantilever assembly was placed in the humidity-sensing cell, a particle of lignin was attached to the cantilever tip using the AFM as a force-controlled micromanipulator, as follows. First, the free resonance of the cantilever was determined. Then, the glass slide prepared with UV-curable adhesive was placed in the AFM, and the cantilever was lowered onto the adhesive, translated a short distance, and then withdrawn. The free resonance of the cantilever plus adhesive was then recorded to quantify the mass of the adhesive. Subsequently, the glass slide prepared with lignin particles was placed in the AFM, and the cantilever with adhesive was lowered onto a lignin particle. Once attached, UV light was used to cure the adhesive and permanently attach the lignin particle to the cantilever tip. The cantilever assembly was then placed in the humidity-sensing cell and positioned in the AFM. Finally, the free resonance frequency of the cantilever with the attached particle was recorded at RH increments for at least two full cycles.

The experimental process was repeated three times using three separate cantilever and particle assemblies. The cantilevers used for the three experimental runs were (All-In-One-Tipless TAP 300, Budget Sensors, Bulgaria) and had measured spring constants (k)

of $\approx$ 48 N/m, $\approx$ 42 N/m, and $\approx$ 39 N/m and fundamental free resonance frequencies (f) of $\approx$ 409 kHz, $\approx$ 406 kHz, and $\approx$ 411 kHz, respectively. The mass measurements were computed by resonating the AFM cantilever and using it as a microbalance, where the shift in resonance frequency relates to the mass of the end load through a simple harmonic oscillator model (Raiteri et al. 2001; Berger et al. 1997; Scandella et al. 1998), as described by:

$$m_l = k\left[\frac{1}{\left(2\pi f_{c,a,l}\right)^2} - \frac{1}{\left(2\pi f_{c,a}\right)^2}\right] \qquad (1)$$

$$m_a = k\left[\frac{1}{\left(2\pi f_{c,a}\right)^2} - \frac{1}{\left(2\pi f\right)^2}\right] \qquad (2)$$

where m_l is the lignin particle mass, m_a is the adhesive mass, and $f_{c,a}$, and $f_{c,a,l}$ are the free resonance of the cantilever plus adhesive and the cantilever plus adhesive and lignin particle, respectively. Table 1 shows the free resonance frequencies and the corresponding mass measurements for each experimental run.

The lignin particle masses for each RH increment were calculated using the corresponding resonance frequency. As RH increases, the change in resonance frequency of the cantilever plus adhesive is minimal compared to the notable decrease in resonance frequency of the cantilever plus adhesive and lignin particle, as shown in Supplementary Fig. 2. Therefore, the decrease in resonance frequency and increase in computed mass were attributed only to the sorption of available moisture in the lignin particle as the RH increased. Using an AFM cantilever as a mass sensor has been known to detect changes in mass on the order of femtograms and even zeptograms (Oden 1998, Berger et al. 1997, Feng et al. 2007), which provides improved sensitivity when determining the change in mass of the lignin particle as RH varies. The moisture content (MC) of the lignin particles was computed for each RH increment according to:

$$MC(\%) = \frac{w}{100} = \frac{m_l - m_{l(dry)}}{m_{l(dry)}} = \frac{m_{H_2O}}{m_{l(dry)}} \qquad (3)$$

where w is the moisture content in g H_2O per g dry material, m_l is the mass of the lignin particle at each RH as calculated in Eq. 1, $m_{l(dry)}$ was taken as the lowest computed mass and, as expected, occurred at

Table 1 Free resonance frequencies and corresponding mass measurements

Experimental run	Free resonance frequency (kHz)		Mass measurement (ng)	
	Cantilever + adhesive ($f_{c,a}$)	Cantilever + adhesive + lignin particle ($f_{c,a,l}$) (minimum)	Adhesive (m_a)	Lignin particle ($m_{l(dry)}$) (minimum)
1	396	323	0.49	3.9
2	393	268	0.43	7.8
3	405	301	0.18	4.9

the lowest RH increment, and m_{H_2O} is the mass of water in the lignin particle.

For the complete range of RH, the semi-empirical GAB model was applied to predict the moisture sorption isotherms of the lignin particle (Volkova et al. 2012; Quirijns et al. 2005; Timmermann et al. 2001; Anderson 1946):

$$w = \frac{w_m C K a_w}{(1 - K a_w)(1 - K a_w + C K a_w)} \quad (4)$$

where w_m is the moisture content of the monolayer of water molecules, C is the Guggenheim constant that is related to the heat of sorption, K is a constant related to the free energy of the additional layers of water molecules, and a_w is the water activity or $RH/100$. Equation 4 was rewritten to perform a non-linear regression analysis using OriginPro 2017 software:

$$w = \frac{B_1 a_w}{1 + B_2 a_w + B_3 a_w^2} \quad (5)$$

$$B_1 = w_m C K \quad (6)$$

$$B_2 = C K - K \quad (7)$$

$$B_3 = K^2 - C K^2 \quad (8)$$

A non-linear least squares analysis, specifically, the Levenberg–Marquardt algorithm, was applied to the first exposure adsorption (Supplementary Information), subsequent cycle readsorption, and all desorption experimental data, respectively. The parameters of the GAB model were subsequently computed and used to develop representative moisture sorption isotherms.

Mapping moisture-dependent nanomechanical contrast with contact resonance force microscopy

In preparation for AFM measurements (Fig. 1), 0.5 mL solution of toluene and 35% poly(tert-butyl acrylate) (PtBA) by mass was dropcast onto a glass slide. Once set, lignin particles were dispersed on the PtBA, and the assembly was placed in an oven at 60 °C for 5400 s to partially embed the lignin particles. PtBA was selected for sample preparation due to its characteristically low glass transition temperature ($T_g \approx 60$ °C) with the purpose of limiting the thermal exposure of lignin to reasonably low temperatures. The AFM cantilever (PPP-FMR, Nanosensors, Switzerland) had a measured spring constant of ≈ 1.7 N/m and a free resonance of ≈ 65.9 kHz.

Contact resonance force microscopy (CR-FM) measurements were completed using the dual AC resonance tracking (DART) capabilities of the MFP-3D AFM (Asylum Research, Santa Barbara, CA) (Rodriguez et al. 2007). CR-FM experimental techniques and analysis are well documented within the literature (Rabe et al. 2000; Rabe 2006; Hurley and Killgore 2013). To summarize, the AFM cantilever is excited over a range of frequencies by an actuator. When the cantilever tip is vibrated in free space, resonant modes occur at certain frequencies depending on the cantilever shape and material. When the cantilever tip is vibrated in contact with the sample surface, the resonant mode occurs at a frequency that is greater than the free resonance frequency due to tip-sample interaction. Using the free and contact resonance frequencies, material properties of the sample can be determined using appropriate models. In this case, the cantilever is modeled as a mass-distributed beam of a finite distance that is fixed at one end (i.e., the clamp) and has a spring at the other end (i.e., the

tip-sample interaction). The model predicts the contact stiffness using the cantilever spring constant and the recorded free and contact resonance frequencies. Images of the surface topography and corresponding contact stiffness can be obtained by continuously recording the contact resonance frequency while scanning the sample surface (Rodriguez et al. 2007).

AFM measurements were performed using the experimental set-up described in "Experimental Set-Up" section. A lignin particle was located using an optical microscope, and a region on the particle surface was identified for measurement. After preconditioning the lignin sample by performing at least one full RH cycle, AFM measurements were taken at 5 increasing and 5 decreasing RH increments for 3 full cycles. At each RH increment, CR-FM with DART measurements generated data by continuously scanning a 5 μm × 5 μm region with 256 lines of resolution.

3D normalized elastic modulus images of the scanned lignin particle were generated using the Asylum Research MFP3D 15.09.112 software. From the lignin surface scan at the lowest (< 1%) RH increment in the first RH cycle, a 2 μm × 1 μm area of the smooth region was used as reference material for the elastic parameters. Thus, all elastic modulus values were normalized with respect to the elastic modulus of the dry and smooth 2 μm × 1 μm area. The 3D images were rendered to show the topography of the scanned region of lignin particle with an overlay of the computed and normalized elastic modulus for the same scanned region.

Quantifying hygromechanical performance with force volume mapping

The lignin sample preparation used for the AFM measurements was the same as described in "Mapping moisture-dependent nanomechanical contrast with contact resonance force microscopy" section. The PS sample was tested as manufactured for nanoindentation (NI) and AFM measurements. The AFM cantilever (PPP-NCHR, Nanosensors, Switzerland) had a measured spring constant of ≈ 28 N/m and a free resonance of ≈ 305.4 kHz. Amplitude modulated intermittent contact mode, commonly referred to as tapping mode, measurements were completed in combination with force volume mapping using an MFP-3D AFM (Asylum Research, Santa Barbara,

CA). NI measurements were completed on the PS sample for calibration using a Hysitron TI 950 Triboindenter (Hysitron, Minneapolis, MN) and a Berkovich tip at 12.5% RH. The array consisted of 100 points spaced 20 μm in both x and y directions. The load function was load-controlled and involved a 5 s. load, 2 s. hold, and 5 s. unload. The indentation modulus was computed using the well-established Oliver-Pharr method for the 95th to 20th percentile of the approach curve.

AFM measurements were performed using the experimental set-up described in "Experimental set-up" section. AFM measurements were taken on polystyrene (PS), as a calibration material, at 8 increasing RH increments. At each RH increment, tapping mode measurements generated a high-resolution image of a 5 μm × 1.25 μm region, and then force-distance curves were taken over a 32 × 8 point map of the same region. After completing calibration measurements, lignin was tested using the same AFM cantilever and experimental set-up. First, a lignin particle was located using the optical microscope, and a region on the surface of the particle was identified for measurement. After preconditioning the lignin sample by performing at least one full RH cycle, AFM measurements were taken at 6 increasing and 6 decreasing RH increments for 3 full cycles. At each RH increment, tapping mode measurements generated a high-resolution image of a 5 μm × 5 μm region, and then force-distance curves were taken over a 32 × 32 point map of the same region. A 1 μm × 1 μm area representing 42 force-distance curves was identified for a smooth and rough domain, respectively, and tracked over all the RH increments.

Using the Asylum Research (AR) MFP3D 15.09.112 software, the Hertz model was selected to compute (1) the elastic modulus of PS from the complete set of 256 force-distance curves and (2) the elastic modulus of lignin from the 42 force-distance curves within the 1 μm × 1 μm area of the smooth domain. In AFM force spectroscopy, the inverse optical lever sensitivity (InvOLS) value is used to convert the measured voltage to cantilever displacement, which is necessary for determining the force value. Typically, InvOLS values are derived from force spectroscopy measurements performed on a hard surface. Therefore, the lowest InvOLS value, corresponding to the stiffest material measurement, was evaluated within the AR software for both lignin and

PS and used as an input parameter to compute elastic modulus from the Hertz model.

The Hertz model does not consider adhesion or surface forces and assumes the tip is a smooth elastic sphere while the sample has a rigid flat surface. To address the model limitations, only an initial section of the approach curve within the elastic regime and over an indentation depth (δ) of 0–5 nm was considered for analysis. The reduced elastic modulus (E^*) can be determined using the Hertz model according to (Johnson and Johnson 1987; Hertz et al. 1896):

$$\delta = \left(\frac{9P^2}{16RE^{*2}}\right)^{1/3} \tag{9}$$

where P is the applied force and R is the radius of spherical tip. A value for R was based on NI and AFM nanomechanical results for PS, which are shown in Supplementary Fig. 8. In summary, the nanomechanical properties of PS were measured using NI at 12.5% RH and AFM at 16.6% RH. The NI result for elastic modulus of PS was used as a known reference value such that a matching value in the AFM Hertzian analysis could be obtained by varying R. Ultimately, a value of 8 nm was selected for R, which is in good accordance with the manufacturer specifications for the probe. For all AFM force-distance curves, E^* from the Hertz model is used to find the elastic modulus of the sample, E, according to:

$$\frac{1}{E^*} = \frac{1 - v^2}{E} + \frac{1 - v_t^2}{E_t} \tag{10}$$

where v and v_t are the Poisson ratios for the sample and cantilever tip, respectively, and E_t is the elastic modulus of the cantilever tip.

Results and discussion

Moisture sorption isotherms

Characteristic experimental moisture sorption isotherms for three lignin particles are shown in Fig. 2, along with previously published data from (Christensen and Kelsey 1958; Cousins 1976; Reina et al. 2001; Volkova et al. 2012), and the GAB model prediction of lignin moisture content for a given RH. For the complete range of RH, the GAB model was fitted to the adsorption and desorption isotherms,
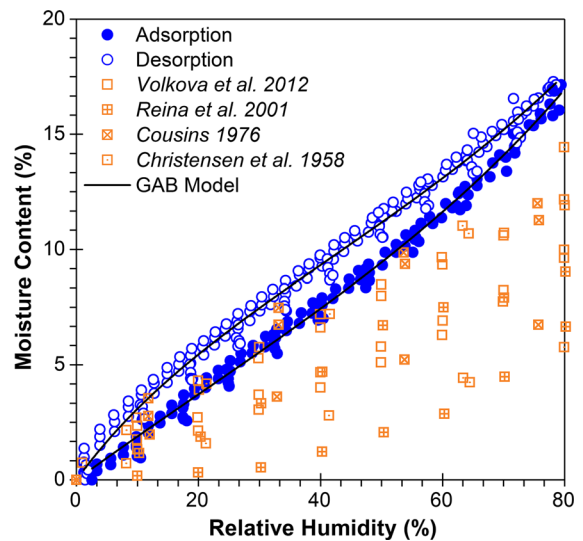

Fig. 2 Moisture sorption isotherms for lignin particles experimentally determined from AFM measurements and previous studies and computationally predicted using the Guggenheim–Anderson–de Boer (GAB) model

respectively. Table 2 shows the goodness-of-fit and the GAB parameters that are descibed by Eqs. 5–8 and found using a non-linear least squares regression analysis. The GAB model demonstrates a close fit of the experimental data with a greater than 0.991 R^2 value for the repeating adsorption and desorption curves. Two of the tested lignin particles were exposed to RH for the first time and demonstrated an observable delay in moisture uptake beyond $\approx$ 30% RH. For reference, the experimental and computational results have been included within Supplementary Fig. 3.

Measuring surface energy can be used to characterize the interaction between materials, which, for example, provides insight into the likelihood of lignin adsorbing moisture. Previous studies have used inverse gas chromatography (IGC) to measure the dispersive component of the surface energy and solubility parameters of lignin (Belgacem et al. 1996; Shen et al. 1998; Ni et al. 2016; Voelke 2017).

Table 2 GAB parameters for experimental moisture sorption isotherms

	w_m	C	K	R^2
Adsorption	0.130	2.538	0.586	0.99404
Desorption	0.115	5.547	0.575	0.99141

Results indicate that lignin will interact with polar compounds (e.g., water molecules) (Voelke 2017), which corresponds to the observed and reported moisture sorption of lignin (Fig. 2).

As shown in Fig. 2, the moisture content of lignin derived from conducted AFM measurements is typically greater than previously reported values for the same RH increment. Although within the same order of magnitude, the variation may be due to the inherent differences in the chemical composition of lignin or the experimental approach. Previous studies have identified differences in the composition of the alkali lignin (CAS Number 8068-05-1, Sigma Aldrich) used in this study compared to other lignins due to source or extraction method using characterization techniques such as standard stuctural analyses methods (Zhang et al. 2008), Fourier-transform infrared spectroscopy (FTIR) (Lee and Deng 2015; Yang et al. 2007), and nuclear magnetic resonance (NMR) (Zhao et al. 2017; Constant et al. 2016). In addition, previous studies have used thermally molded lignin specimens (Cousins 1976) and different measurement techniques, such as dynamic vapor sorption (Volkova et al. 2012) or gravimetric (Reina et al. 2001; Cousins 1976; Christensen and Kelsey 1958) measurements, to characterize the moisture sorption properties of lignin. For this study, using the AFM cantilever as a mass sensor to acquire mass moisture measurements has notable advantages over other methods. First, lignin particles are tested in their virgin state and do not undergo additonal sample preparation or processing prior to testing. Second, data obtained herein via AFM are on the same particle length scale and in identical environmental conditions as the subsequent nanomechanical characterization.

The GAB model parameters, w_m, C, and K, have physical meanings that provide insight into the water vapor sorption by lignin particles. The parameter w_m describes the availablility of sites for water sorption by the material surface. C and K are energy constants that describe the energy difference between the first and upper layers of water molecules and the upper layers and liquid water, respectively. Larger C values correspond to greater strength of the water bound in the first layer, while K describes the number of sorbed water molecules arranged in the multilayer structure (Quirijns et al. 2005; Timmermann et al. 2001).

The moisture sorption isotherms (Fig. 2) for three lignin particles over increasing and decreasing RH cycles are (1) in good agreement and (2) well characterized using the GAB model. As RH increases from 0% to (78.8 ± 0.8)%, the moisture content of a lignin particle reaches (17.4 ± 0.8)%. Conversely, as RH decreases to (1.3 ± 0.2)%, the moisture content returns to (0.6 ± 0.6)%. The w_m values (Table 2) for adsorption and desorption isotherms are comparable and, correspondingly, there may be a comparable capacity of the monolayer for those cases, which may explain the return to a similar moisture content at ≈ 0% RH. The higher C value (Table 2) for the desorption compared to the adsorption isotherm suggests that the monolayer of water molecules is more tightly bound, which may explain the lag (i.e., hysteresis) in returning to the same moisture content for the same RH increment. Comparatively, Volkova et al. (2012) also reported a hysteretic trend in moisture content as RH increased and decreased, as shown in Fig. 2.

Moisture induced nanomechanical contrast of the lignin particle surface

CR-FM measurements were used to render the lignin particle images in Fig. 3, which show a 5 μm × 5 μm region of the surface topography with a normalized elastic modulus overlay for 3 RH increments and 3 RH cycles. Before AFM measurements, the lignin sample was subjected to at least one full RH cycle, thus the lignin particle is expected to follow the repeatable sorption isotherms presented in Fig. 2. As shown in Fig. 3, lignin at RH < 1% in RH Cycle 1 exhibits a discernable topographical heterogeneity in the form of smooth and rough domains. In a previous study, scanning electron microscopy images show smooth and rough domains on the lignin surface at the micron length scale (Ibrahim et al. 2010). The heterogeneity is further substantiated by a difference in mechanical response to moisture. For comparison, all data were normalized with respect to the elastic modulus the dry (< 1% RH) and smooth domain, as described in "Mapping moisture-dependent nanomechanical contrast with contact resonance force microscopy" section. Additional rendered images of the particle during RH Cycle 1, which show the normalized elastic modulus and the lignin particle topography and are shown in Supplementary Fig. 4.

As RH increases from < 1% to (76 ± 1)% over RH Cycle 1 (Fig. 3), there is noticeable softening, as

Fig. 3 Nanomechanical contrast images of a lignin particle surface exposed to moisture using AFM contact resonance force microscopy (CR-FM) measurements. The computed elastic modulus is normalized with respect to a 2 μm × 1 μm area of the smooth region from RH Cycle 1 and RH < 1%, which is represented by the dotted rectangular outline
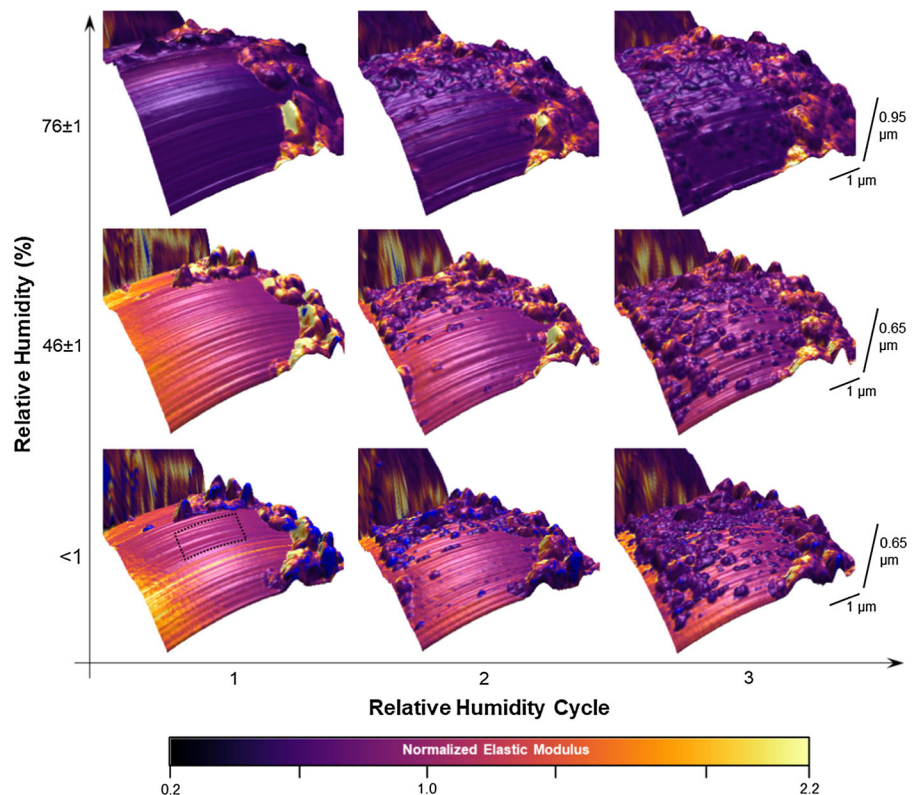
indicated by a decrease in both computed normalized elastic modulus and measured frequency. As RH increases from < 1% to (76 ± 1)% for the 2 μm × 1 μm area of the smooth domain, the CR frequency decreases from (326 ± 0.8) to (318 ± 2.7) kHz which correlates to a 34% decrease in the normalized elastic modulus from (1.0 ± 0.057) to (0.66 ± 0.088). Since the elastic modulus is normalized with respect to the 2 μm × 1 μm area of the smooth domain at < 1% RH, a value of 1.0 is expected, but the standard deviations have been provided to denote the degree of variability. More broadly, for the entire 5 μm × 5 μm scanned region, the normalized elastic modulus decreases 46% from (1.5 ± 12.4) to (0.84 ± 0.92) as RH increases from < 1% to (76 ± 1)%, which demonstrates an overall moisture-induced reduction in mechanical stiffness. The average normalized elastic modulus values of 1.5 and 0.84 show that the rough domains do contribute to an overall increase in elastic modulus by 50% and 27%, respectively. However, at < 1% and (76 ± 1)% RH the standard deviation increases from 0.057 to 12.4 and from 0.088 to 0.92 for the smooth domain and the entire area, respectively.

The degree of variability introduced by the rough domains may be attributed to increased noise in the AFM measurements due to the effect of topographical height change on contact area between the tip and sample surface. This increased variablity in the rough domains indicates that softening is most quantifiable in the smooth domains, which have comparatively tighter distributions.

For RH Cycles 2 and 3, AFM measurements suggest a recovery in normalized elastic modulus at < 1% RH as shown in Fig. 3. Comparing the transition in RH from (76 ± 1)% to < 1% between RH Cycles 1 and 2 and RH Cycles 2 and 3, the computed normalized elastic modulus increases by 54% from (0.66 ± 0.088) to (1.02 ± 0.21) and by 26% from (0.65 ± 0.076) to (0.81 ± 0.30), respectively, for the 2 μm × 1 μm area of the smooth domain. The increases indicate a recovery in material properties as RH transitions from the high to low regimes.

Continuous AFM scanning and tip-sample interaction appear to induce damage to the material surface (Fig. 3) at elevated RH. The smooth domains appear

to be more susceptible to surface damage from AFM scanning when compared to the rough domains. Additionally, the damaged surface exhibits a lower normalized elastic modulus than the visible smooth domain as indicated by the 19% decrease in computed normalized elastic modulus when comparing the RH < 1% scans for RH Cycles 1 and 3. Therefore, the accumulated damage from CR-FM measurements reduces confidence in quantifying and comparing the nanomechancial behavior across RH cycles. Lastly, after the experimental run, a 10 μm × 10 μm image was taken, which showed that the accumulated surface damage was limited to the scanned region and therefore not a result of changing RH. Quantification of this accumulated damage is available as part of the Supplementary Information.

Nanomechanical characterization of heterogenous lignin domains using AFM Force spectroscopy as it relates to moisture content

The hygromechanical response of the heterogenous smooth and rough topographical domains described in "Moisture induced nanomechanical contrast of the lignin particle surface" section has been further investigated using AFM force spectroscopy (Figs. 4, 5, and 6). The blue, orange, and green color scheme in Figs. 4, 5, and 6 correspond to increasing moisture content from 0.024 to 9.05 to 17.33% and relates to 0.122, 48.1, and 81.2% RH through the GAB-modeled

sorption curve, respectively. For all force spectroscopy measurements, the lignin sample had been exposed to at least one full RH cycle before data collection, thus the water sorption is expected to follow the repeatable adsorption and desorption isotherms presented in Fig. 2.

High resolution imaging

Figure 4 shows tapping mode images of the topographic slope along the fast-scan direction for a 5 μm × 5 μm area of the lignin surface for three increasing RH increments. Topographic slope was used instead of raw-topography to emphasize the rough and smooth regions while minimizing the influence of large-scale surface curvature. Similar to Fig. 3, the AFM images in Fig. 4 substantiate the presence of a discernable topographical heterogeneity in the form of smooth and rough domains on the lignin surface.

For three RH values, one smooth 1 μm × 1 μm area (S1, S2, and S3) and one rough 1 μm × 1 μm area (R1, R2, and R3) of the lignin surface were tracked and analyzed, as shown in Fig. 4a, b, c, respectively. As expected, surface damage due to tapping mode measurements in the smooth domains is negligible, since the applied force was significantly smaller compared to CR-FM. However, surface damage due to the force spectroscopy indents is observed in the smooth domains of the lignin surface as
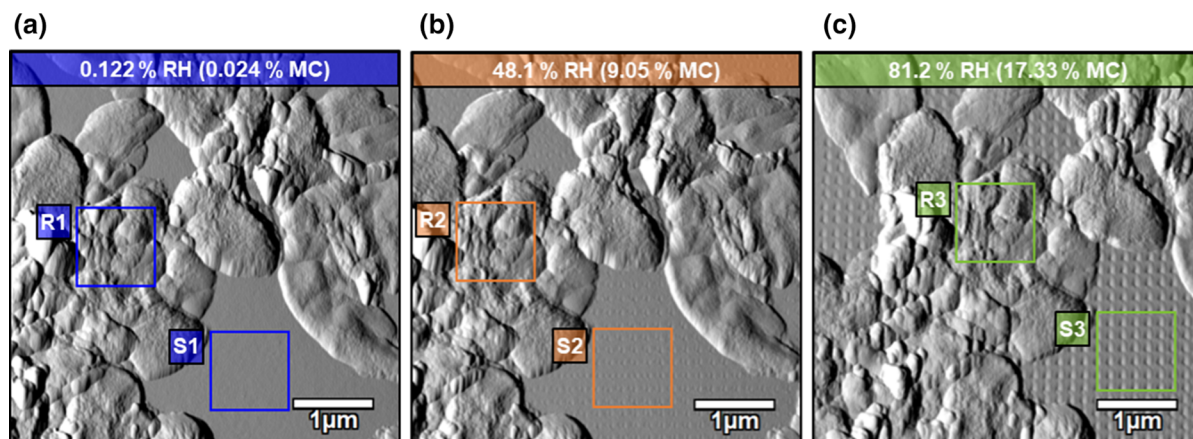

Fig. 4 AFM tapping mode images of the topographic slope for a 5 μm × 5 μm region of the lignin surface as RH increases from **a** 0.122% to, **b** 48.1% to, **c** 81.2%. A 1 μm × 1 μm area of the smooth and rough topographical domain is denoted as S1 and R1, S2 and R2, and S3 and R3 in **a**, **b**, and **c**, respectively.

The change in topographical height over a discrete horizontal distance (i.e., slope) was used to depict surface roughness where—60 nm/nm is black and 50 nm/nm is white. (Color figure online)
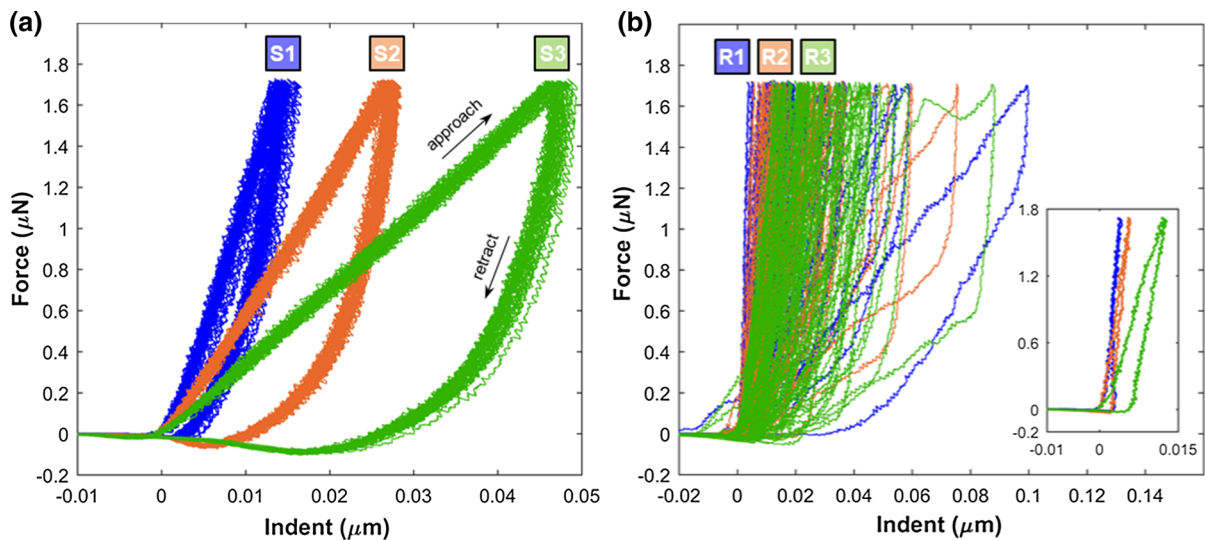
Fig. 5 Nanoscale characterization using AFM force volume mapping of a 1 μm × 1 μm smooth **a** and rough **b** topographical area of the lignin surface which corresponds to S1 and R1, S2 and R2, and S3 and R3 in Fig. 4a, b, and c, respectively. The moisture content of the lignin particle is 0.024% (blue color), 9.05% (orange color), and 17.33% (green color). The inset in **b** shows the front force-distance curve for each moisture content. (Color figure online)
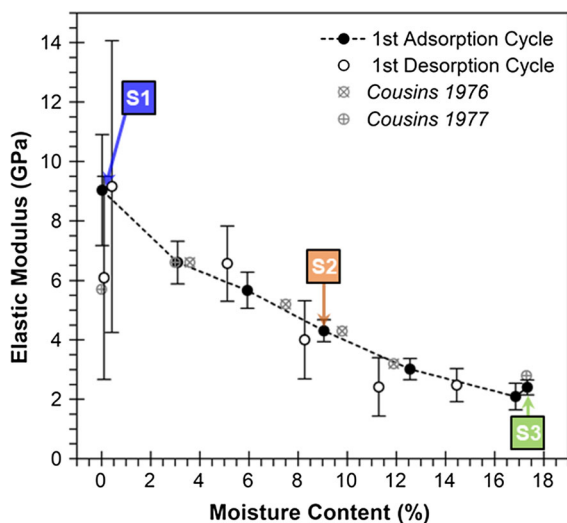
Force volume mapping

For varying moisture content, the smooth and rough heterogeneous domains of the lignin particle surface were characterized using AFM force volume mapping, as shown in Fig. 5a and b, respectively. Figure 5a shows excellent repeatability for 42 force-distance curves taken over the corresponding 1 μm × 1 μm smooth area at each moisture content, described as S1, S2, and S3 in Fig. 4a, b, and c, respectively. As RH increases from S1 to S2 to S3, the slope of the approach curve decreases and the area between the approach and the retract curves increases. The decreasing slope correlates to a decrease in material stiffness due to the presence of added moisture. The increasing area between the curves correlates to an increase in energy dissipation, which can be attributed to a viscoelastic response and permanent plastic deformation (Cappella 2016). The permanent deformation (Fig. 5a) presents as the visible indent marks (Fig. 4). Compared to the linear response when using CR-FM (Fig. 3), the force spectroscopy indents (Fig. 5) depress further into the sample surface, which provides a greater understanding of the nonlinear plastic response of lignin as moisture content increases. It is suggested that the water molecules act as a plasticizer in this case, and increasing the

Fig. 6 Elastic modulus as it relates to moisture content. Elastic modulus values were computed using the Hertz method for a 1 μm × 1 μm area of the smooth domain over one full RH cycle. The blue, orange, and green drop bars correspond to S1, S2, and S3 in Fig. 4a, b, and c, respectively, and the force-distance curves in Fig. 5a. (Color figure online)

moisture content increases. In contrast, no apparent surface damage from AFM measurements was observed in the rough domains as moisture content increases. This suggests that the rough domains are more resistant to damage from AFM measurements.

water content decreases stiffness and increases plasticity by interacting with the polymer chains or creating free volume (Hariri et al. 2012; Bouajila et al. 2006).

Compared to the smooth domain, Fig. 5b shows disparity between the 42 force-distance curves taken over the corresponding 1 μm × 1 μm rough area at each moisture content, described as R1, R2, and R3 in Fig. 4a, b, and c, respectively. At each moisture content, there are examples of curves with low or high stiffness (decreased or increased slope) and high or low energy dissipation (increased or decreased area between the curves), respectively. For example, the curve with the lowest stiffness (greatest slope) is from the lowest moisture content, which demonstrates atypical behavior compared to the smooth domain force-distance curves. The disparity in force-distance measurements may be attributed to either topographical or compositional variation. Variable surface topography (roughness) can affect the contact area between the surface and cantilever tip during force curve measurements, while varying chemical composition can affect the material response due to the relationship between polymer structure and property. However, despite the observed disparity, there is a decrease in maximum stiffness (i.e., slope) as moisture content increases from 0.024 to 9.05 to 17.54%, as shown in the Fig. 5b inset, which demonstrates a general trend towards softening in the rough domain.

The difference in topographical features and hygromechanical response between the heterogeneous smooth and rough domains suggests a corresponding difference in chemical composition. Lignin is well known to be comprised of three major structures: hydroxyphenyl, guaiacyl, and syringyl phenylpropanoid units (Faruk and Sain 2016; Ragauskas et al. 2014; Boerjan et al. 2003; Hatakeyama and Hatakeyama 2009; Sarkanen and Ludwig 1971). A previous study (Ciesielski et al. 2014) suggests that lignin with high concentrations of guaiacyl or syringyl units has a corresponding effect on the stiffness and therefore the elastic modulus of the material. The extraction process to obtain lignin from its lignocellulosic source may create regions with different concentrations of the major structures in lignin, which may result in the topographical and hygromechanical heterogeneity identified through AFM measurements.

Quantifying the elastic modulus of the smooth domain

For the first adsorption and first desorption cycle, Fig. 6 shows the computed elastic modulus using the Hertz model for the tracked 1 μm × 1 μm smooth area at each moisture content. For reference, S1, S2, and S3 have been identified in Fig. 6 and correspond to Fig. 4a, b, and c, respectively, and the force-distance curves shown in Fig. 5a. As the moisture content increases from 0.024% (S1) to 9.05% (S2) to 17.33% (S3), the elastic modulus decreases from (9.0 ± 1.87) GPa to (4.3 ± 0.37) GPa to (2.4 ± 0.25) GPa. As RH and moisture content subsequently decrease, the elastic modulus rebounds in magnitude, which was also observed in Fig. 3 using CR-FM. In addition, the low RH force-distance curves for subsequent cycles, as shown in Supplementary Fig. 7, demonstrate less plasticity and greater stiffness than the high RH force-distance curves, which also indicates a rebound in elastic modulus. This evidence of material property recovery confirms that the mechanical softening is a direct result of moisture content and not an artifact of damage due to force volume mapping. However, the increase in standard deviation for computed elastic modulus and greater variablity in subsequent RH cycle force-distance curves implies less accuracy in collected mechanical property data and may indicate accumulated surface damage. Consequently, it is suggested that, in this case, the computed elastic moduli for the first adsorption cycle provide a better quantification of the hygromechancial properties. The complete set of elastic modulus data computed using the Hertz model for all three RH cycles is available in Supplementary Table 3, as a reference.

The current study reports similar elastic moduli for each moisture content compared to previous studies (Cousins 1976, 1977), except at low (< 1%) moisture content where the elastic modulus reported herein has a 58% higher value. It is notable that similar results were obtained between studies despite (1) inevitable variation in the composition of lignin due to source or extraction method (Zhang et al. 2008; Lee and Deng 2015; Zhao et al. 2017; Constant et al. 2016; Yang et al. 2007) and (2) key differences in experimental methods. Compared to previous mechanical characterization (Cousins 1976, 1977), this study presents AFM data for moisture sorption isotherms and nanomechanical characterization are on the same particle length scale and subjected to the same RH

conditions, which provides consistency across the results. In addition, the AFM data is collected for more RH increments and over multiple RH cycles offering a more comprehensive representation of the hygromechanical response. The current study also does not use any material processing techniques, such as heat molding, during sample preparation to prevent its effect on the results. Lasly, in contrast to previously used macroscale destructive mechanical testing, this study uses modern nanoscale AFM techniques for mechanical characterization.

Conclusions

In this work, three AFM techniques were used to characterize and relate the moisture sorption and hygromechanical behavior of alkali lignin (CAS Number 8068-05-1, Sigma Aldrich) on the nanoscale. Leveraging multiple AFM techniques provides a more comprehensive material characterization (Passeri et al. 2013). Since all measurements within this study are performed using same AFM experimental set-up, the subsequent results are (1) on a comparable particle length scale and (2) obtained from the same RH environment.

For the first AFM technique, the AFM cantilever was used as a mass sensor to detect the change in moisture content of a lignin particle over three cycles of RH. The collected data were used to develop experimental moisture sorption isotherms for lignin, which were then computationally predicted using the GAB model. For the second AFM technique, CR-FM measurements were taken for three cycles of RH to identify nanomechanical contrast on the lignin surface in response to moisture. The CR-FM scans revealed topographical heterogeneity of the lignin surface described in terms of smooth and rough domains. A notable softening of the lignin surface, especially in the smooth domain, occurred as RH increases, and a recovery in mechanical properties was observed as RH decreases, as described by corresponding shifts in the normalized elastic modulus. For the third AFM technique, force spectroscopy was conducted over a 5 μm × 5 μm region of the lignin surface at 6 RH increments for 3 cycles. In the tapping mode images, the heterogenous lignin surface in terms of smooth and rough domains was again observed. For a 1 μm × 1 μm region of the smooth domain, the force-distance

curves were analyzed using the Hertz method to compute elastic modulus of lignin as it relates to moisture content. The average computed elastic modulus decreased from 9.0 to 4.3 to 2.4 GPa as the moisture content increased from 0.024 to 9.1 to 17.3%, respectively. A discernable recovery in mechanical properties as moisture content subsequently decreased confirms the moisture dependence of mechanical softening.

This work presents valuable experimental results using AFM techniques that correlate moisture content to the nanomechanical properties, namely elastic modulus, of extracted lignin. As the supply of lignin from industrial waste streams increases, the hygromechancial behavior of lignin described herein will contribute to the growing effort to develop products and technology (Bajpai 2017; Faruk and Sain 2016; Lupoi et al. 2015; Ragauskas et al. 2014; Yiamsawas et al. 2014; Brodin et al. 2012; Faria et al. 2012; Lora 2008) that valorize this biorenewable resource.

Compliance with ethical standards

Conflicts of interest The authors declare that they have no conflicts of interest.

References

Anderson RB (1946) Modifications of the Brunauer, Emmett and Teller equation II. J Am Chem Soc 68(4):686–691. https://doi.org/10.1021/ja01208a049

Bajpai P (2017) Carbon fibre from Lignin. Springer, Singapore. https://doi.org/10.1007/978-981-10-4229-4

Belgacem MN, Blayo A, Gandini A (1996) Surface characterization of polysaccharides, lignins, printing ink pigments, and ink fillers by inverse gas chromatography. J Colloid

Interface Sci 182(2):431–436. https://doi.org/10.1006/jcis.1996.0484

Berger R, Gerber C, Lang HP, Gimzewski JK (1997) Micromechanics: a toolbox for femtoscale science: "towards a laboratory on a tip". Microelectron Eng 35(1):373–379. https://doi.org/10.1016/S0167-9317(96)00201-8

Binnig G, Quate CF, Gerber C (1986) Atomic force microscope. Phys Rev Lett 56(9):930–933. https://doi.org/10.1103/physrevlett.56.930

Boerjan W, Ralph J, Baucher M (2003) Lignin biosynthesis. Annu Rev Plant Biol 54(1):519–546. https://doi.org/10.1146/annurev.arplant.54.031902.134938

Bouajila J, Dole P, Joly C, Limare A (2006) Some laws of a lignin plasticization. J Appl Polym Sci 102(2):1445–1451. https://doi.org/10.1002/app.24299

Brodin I, Ernstsson M, Gellerstedt G, Sjöholm E (2012) Oxidative stabilisation of kraft lignin for carbon fibre production. Holzforschung 66(2):141–147. https://doi.org/10.1515/HF.2011.133

Cappella B (2016) Mechanical properties of polymers measured through AFM force–distance curves. Springer, Cham. https://doi.org/10.1007/978-3-319-29459-9

Célino A, Fréour S, Jacquemin F, Casari P (2014) The hygroscopic behavior of plant fibers: a review. Front Chem 1:43. https://doi.org/10.3389/fchem.2013.00043

Charlier L, Mazeau K (2012) Molecular modeling of the structural and dynamical properties of secondary plant cell walls: influence of lignin chemistry. J Phys Chem B 116(14):4163–4174. https://doi.org/10.1021/jp300395k

Chirkova J, Andersons B, Andersone I (2009) Study of the structure of wood-related biopolymers by sorption methods. BioResources 4(3):1044–1057. https://doi.org/10.15376/biores.4.3.1044-1057

Christensen GN, Kelsey KE (1958) The sorption of water vapour by the constituents of wood: determination of sorption isotherms. Aust J Appl Sci 9(3):265–282

Ciesielski PN, Resch MG, Hewetson B, Killgore JP, Curtin A, Anderson N, Donohoe BS (2014) Engineering plant cell walls: tuning lignin monomer composition for deconstructable biofuel feedstocks or resilient biomaterials. Green Chem 16(5):2627. https://doi.org/10.1039/c3gc42422g

Constant S, Wienk HLJ, Frissen AE, de Peinder P, Boelens R, van Es DS, Bruijnincx PCA (2016) New insights into the structure and composition of technical lignins: a comparative characterisation study. Green Chem 18(9):2651–2665. https://doi.org/10.1039/C5GC03043A

Costello H (2017) Lignin products global market size, sales data 2017–2022 & applications in animal feed industry (Market Analysis No. 188450). Orbis Research, Dallas. Retrieved from https://marketersmedia.com/lignin-products-global-market-size-sales-data-2017-2022-applications-in-animal-feed-industry/188450. Accessed 16 Nov 2017

Cousins WJ (1976) Elastic modulus of lignin as related to moisture content. Wood Sci Technol 10(1):9–17

Cousins WJ (1977) Elasticity of isolated lignin: young's modulus by a continuous indentation method. NZ J For Sci 7(1):107–112

Engelund ET (2011) Wood-water interactions. Dissertation, Technical University of Denmark, Kgs. Lyngby

Fang Z, Smith RL (2016) Production of biofuels and chemicals from lignin. Springer, Singapore. https://doi.org/10.1007/978-981-10-1965-4

Farahi RH, Charrier AM, Tolbert A, Lereu AL, Ragauskas A, Davison BH, Passian A (2017) Plasticity, elasticity, and adhesion energy of plant cell walls: nanometrology of lignin loss using atomic force microscopy. Sci Rep 7(1):152. https://doi.org/10.1038/s41598-017-00234-4

Faria FA, Evtuguin DV, Rudnitskaya A, Gomes MT, Oliveira JA, Graça MPF, Costa LC (2012) Lignin-based polyurethane doped with carbon nanotubes for sensor applications. Polym Int 61(5):788–794. https://doi.org/10.1002/pi.4140

Faruk O, Sain M (2016) Lignin in polymer composites. William Andrew, Oxford

Feng XL, He R, Yang P, Roukes ML (2007) Very high frequency silicon nanowire electromechanical resonators. Nano Lett 7(7):1953–1959. https://doi.org/10.1021/nl0706695

Fengel D, Wegener G (1983) Lignin. In: Fengel D, Wegener G (eds) Wood: chemistry, ultrastructure, reactions. Walter de Gruyter, Berlin, pp 132–181. https://doi.org/10.1515/9783110839654

Gandini A, Belgacem MN (2008) Lignins as components of macromolecular materials. In: Monomers, polymers and composites from renewable resources, pp 243–271. Elsevier, Amsterdam. Retrieved from https://www.sciencedirect.com/science/article/pii/B9780080453163000119. Accessed 16 Nov 2017

Gellerstedt G, Henriksson G (2008) Lignins: major sources, structure and properties. In: Belgacem MN, Gandini A (eds) Monomers, polymers and composites from renewable resources, pp 201–224. Elsevier, Amsterdam. Retrieved from https://www.sciencedirect.com/science/article/pii/B9780080453163000090

Hariri HH, Lehaf AM, Schlenoff JB (2012) Mechanical properties of osmotically stressed polyelectrolyte complexes and multilayers: water as a plasticizer. Macromolecules 45(23):9364–9372. https://doi.org/10.1021/ma302055m

Hatakeyama H, Hatakeyama T (2009) Lignin structure, properties, and applications. In: Abe A, Dusek K, Kobayashi S (eds) Biopolymers. Springer, Berlin, pp 1–63. https://doi.org/10.1007/12_2009_12

Hatakeyama T, Hirose S, Hatakeyama H (1983) Differential scanning calorimetric studies on bound water in 1, 4-dioxane acidolysis lignin. Macromol Chem Phys 184(6):1265–1274

Hertz H, Jones DE, Schott GA (1896) Miscellaneous Papers. Macmillan and Company, London

Hurley DC, Killgore JP (2013) Dynamic contact AFM methods for nanomechanical properties. Scanning Probe Microsc Ind Appl. https://doi.org/10.1002/9781118723111.ch5

Ibrahim MM, Agblevor FA, El-Zawawy WK (2010) Isolation and characterization of cellulose and lignin from steam-exploded lignocellulosic biomass. BioResources 5(1):397–418. https://doi.org/10.15376/biores.5.1.397-418

Johnson KL, Johnson KL (1987) Contact mechanics. Cambridge University Press, Cambridge

Kulasinski K, Guyer R, Derome D, Carmeliet J (2015) Water adsorption in wood microfibril-hemicellulose system: role of the crystalline–amorphous interface.

Biomacromolecules 16(9):2972–2978. https://doi.org/10.1021/acs.biomac.5b00878

Lee A, Deng Y (2015) Green polyurethane from lignin and soybean oil through non-isocyanate reactions. Eur Polym J 63:67–73. https://doi.org/10.1016/j.eurpolymj.2014.11.023

Lora J (2008) Industrial commercial lignins: sources, properties and applications. In: Belgacem MN Gandini A (eds) Monomers, polymers and composites from renewable resources, pp 225–241. Elsevier, Amsterdam. Retrieved from https://www.sciencedirect.com/science/article/pii/B9780080453163000107. Accessed 16 Nov 2017

Lupoi JS, Singh S, Parthasarathi R, Simmons BA, Henry RJ (2015) Recent innovations in analytical methods for the qualitative and quantitative assessment of lignin. Renew Sustain Energy Rev 49:871–906. https://doi.org/10.1016/j.rser.2015.04.091

Maivald P, Butt HJ, Gould SAC, Prater CB, Drake B, Gurley JA, Hansma PK (1991) Using force modulation to image surface elasticities with the atomic force microscope. Nanotechnology 2(2):103. https://doi.org/10.1088/0957-4484/2/2/004

Ni H, Ren S, Fang G, Ma Y (2016) Determination of alkali lignin solubility parameters by inverse gas chromatography and Hansen solubility parameters. BioResources 11(2):4353–4368. https://doi.org/10.15376/biores.11.2.4353-4368

Oden PI (1998) Gravimetric sensing of metallic deposits using an end-loaded microfabricated beam structure. Sens Actuators B Chem 53(3):191–196. https://doi.org/10.1016/S0925-4005(98)00339-6

Passeri D, Rossi M, Tamburri E, Terranova ML (2013) Mechanical characterization of polymeric thin films by atomic force microscopy based techniques. Anal Bioanal Chem 405(5):1463–1478. https://doi.org/10.1007/s00216-012-6419-3

Quirijns EJ, van Boxtel AJ, van Loon WK, van Straten G (2005) Sorption isotherms, GAB parameters and isosteric heat of sorption. J Sci Food Agric 85(11):1805–1814. https://doi.org/10.1002/jsfa.2140

Rabe U (2006) Atomic force acoustic microscopy. In: Bhushan B, Fuchs H (eds) Applied scanning probe methods II. Springer, Berlin, pp 37–90

Rabe U, Amelio S, Kester E, Scherer V, Hirsekorn S, Arnold W (2000) Quantitative determination of contact stiffness using atomic force acoustic microscopy. Ultrasonics 38(1):430–437. https://doi.org/10.1016/S0041-624X(99)00207-3

Ragauskas AJ, Beckham GT, Biddy MJ, Chandra R, Chen F, Davis MF, Wyman CE (2014) Lignin valorization: improving lignin processing in the biorefinery. Science 344(6185):1246843. https://doi.org/10.1126/science.1246843

Raiteri R, Grattarola M, Butt H-J, Skládal P (2001) Micromechanical cantilever-based biosensors. Sens Actuators B Chem 79(2):115–126. https://doi.org/10.1016/S0925-4005(01)00856-5

Reina JJ, Dominguez E, Heredia A (2001) Water sorption-desorption in conifer cuticles: the role of lignin. Physiol Plant 112(3):372–378. https://doi.org/10.1034/j.1399-3054.2001.1120310.x

Rodriguez BJ, Callahan C, Kalinin SV, Proksch R (2007) Dual-frequency resonance-tracking atomic force microscopy. Nanotechnology 18(47):475504. https://doi.org/10.1088/0957-4484/18/47/475504

Rosa-Zeiser A, Weilandt E, Hild S, Marti O (1997) The simultaneous measurement of elastic, electrostatic and adhesive properties by scanning force microscopy: pulsed-force mode operation. Meas Sci Technol 8(11):1333. https://doi.org/10.1088/0957-0233/8/11/020

Sannigrahi P, Ragauskas AJ (2011) Characterization of fermentation residues from the production of bio-ethanol from lignocellulosic feedstocks. J Biobased Mater Bioenergy 5(4):514–519. https://doi.org/10.1166/jbmb.2011.1170

Sannigrahi P, Pu Y, Ragauskas A (2010) Cellulosic biorefineries—unleashing lignin opportunities. Curr Opin Environ Sustain 2(5):383–393. https://doi.org/10.1016/j.cosust.2010.09.004

Sarkanen KV, Ludwig CH (1971) Lignins: occurrence, formation, structure and reactions. Wiley-Interscience, New York

Scandella L, Binder G, Mezzacasa T, Gobrecht J, Berger R, Lang HP, Jansen JC (1998) Combination of single crystal zeolites and microfabrication: two applications towards zeolite nanodevices. Microporous Mesoporous Mater 21(4):403–409. https://doi.org/10.1016/S1387-1811(98)00021-3

Shen W, Parker IH, Sheng YJ (1998) The effects of surface extractives and lignin on the surface energy of eucalypt kraft pulp fibres. J Adhes Sci Technol 12(2):161–174. https://doi.org/10.1163/156856198X00038

Thakur VK, Thakur MK, Raghavan P, Kessler MR (2014) Progress in green polymer composites from lignin for multifunctional applications: a review. ACS Sustain Chem Eng 2(5):1072–1092. https://doi.org/10.1021/sc500087z

Timmermann EO, Chirife J, Iglesias HA (2001) Water sorption isotherms of foods and foodstuffs: BET or GAB parameters? J Food Eng 48(1):19–31. https://doi.org/10.1016/S0260-8774(00)00139-4

Troyon M, Wang Z, Pastre D, Lei HN, Hazotte A (1997) Force modulation microscopy for the study of stiff materials. Nanotechnology 8(4):163. https://doi.org/10.1088/0957-4484/8/4/002

Uraki Y, Koda K (2015) Utilization of wood cell wall components. J Wood Sci 61(5):447–454. https://doi.org/10.1007/s10086-015-1492-9

Vairac P, Cretin B (1998) Frequency shift of a resonating cantilever in a.c. force microscopy: towards a realistic model. Appl Phys A 66(1):S227–S230. https://doi.org/10.1007/s003390051135

Voelke A, Strzemiecka B, Adamska K, Klapiszewski Ł (2017) Surface characterization of lignin materials by means of inverse gas chromatography. In: Northwood DO, Rang T, De Hosson J, Brebbia CA (eds) Materials and contact characterisation VIII, Vol 116, pp 195–203. WIT Press, Boston. Retrieved from http://library.witpress.com/viewpaper.asp?pcode=MC17-020-1. Accessed 28 July 2018

Volkova N, Ibrahim V, Hatti-Kaul R, Wadsö L (2012) Water sorption isotherms of Kraft lignin and its composites.

Carbohydr Polym 87(2):1817–1821. https://doi.org/10.1016/j.carbpol.2011.10.001

Vu T, Chaffee A, Yarovsky I (2002) Investigation of lignin-water interactions by molecular simulation. Mol Simul 28(10–11):981–991. https://doi.org/10.1080/0892702040 00002610

Yang H, Yan R, Chen H, Lee DH, Zheng C (2007) Characteristics of hemicellulose, cellulose and lignin pyrolysis. Fuel 86(12):1781–1788. https://doi.org/10.1016/j.fuel.2006.12.013

Yiamsawas D, Baier G, Thines E, Landfester K, Wurm FR (2014) Biodegradable lignin nanocontainers. RSC Adv. 4(23):11661–11663. https://doi.org/10.1039/C3RA47971D

Youssefian S, Jakes JE, Rahbar N (2017) Variation of nanostructures, molecular interactions, and anisotropic elastic moduli of lignocellulosic cell walls with moisture. Sci Rep 7:2054. https://doi.org/10.1038/s41598-017-02288-w

Zhang B, Huang H-J, Ramaswamy S (2008) Reaction kinetics of the hydrothermal treatment of lignin. Appl Biochem Biotechnol 147(1–3):119–131. https://doi.org/10.1007/s12010-007-8070-6

Zhao W, Xiao L-P, Song G, Sun R-C, He L, Singh S, Cheng G (2017) From lignin subunits to aggregates: insights into lignin solubilization. Green Chem 19(14):3272–3281. https://doi.org/10.1039/C7GC00944E